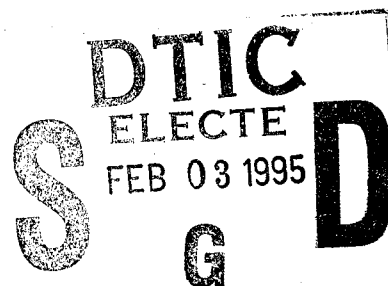
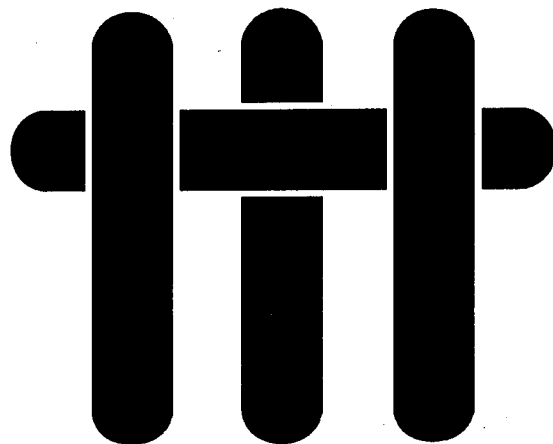



M A T E R I A L S



Crystallization Behavior and Microstructure Evolution of $(Al,Fe)_2O_3$ Synthesized from Liquid Precursors

Andrew D. Polli, Fred F. Lange, and Carlos G. Levi

High Performance Composites Center
Materials Department
College of Engineering
University of California at Santa Barbara


to be submitted for publication to

Journal of the American Ceramic Society

December, 1994

Accession For	
NTIS CRA&I	<input checked="" type="checkbox"/>
DTIC TAB	<input type="checkbox"/>
Unannounced	<input type="checkbox"/>
Justification	<i>per ltr</i>
By _____	
Distribution /	
Availability Codes	
Dist	Avail and/or Special
<i>A-1</i>	

DISTRIBUTION STATEMENT A

Approved for public release;
Distribution Unlimited

19950130 062

DTIC QUALITY INSPECTED 1

Crystallization Behavior and Microstructure Evolution of $(\text{Al,Fe})_2\text{O}_3$ Synthesized from Liquid Precursors

by

Andrew D. Polli, Fred F. Lange, and Carlos G. Levi[†]

ABSTRACT

Aqueous solutions of Al^{3+} and Fe^{3+} nitrates were used to produce $(\text{Al,Fe})_2\text{O}_3$ amorphous solid solutions with up to 50 mole% Fe_2O_3 . Following subsequent heat treatments, all compositions first crystallized to $\gamma(\text{Al,Fe})_2\text{O}_3$ and those with $\geq 20\% \text{Fe}_2\text{O}_3$ ultimately partitioned into a mixture of Al_2O_3 - and Fe_2O_3 -rich α phases as predicted by the equilibrium diagram. There were, however, several possible transformation paths between the γ phase and the final microstructure. Compositions with 10 and 20% Fe_2O_3 both formed an extended α solid solution which partitioned only sluggishly at 1100°C . In contrast, powders with compositions above 30% Fe_2O_3 formed an intermediate metastable orthorhombic phase (O) based on the equiatomic AlFeO_3 compound, but also decomposed eventually into the mixture of two α phases. It appears that the α mixture may evolve directly from γ for compositions near 30% Fe_2O_3 , but clearly forms from O as the Fe content increases. Resistance to partitioning also reaches a minimum at $\sim 30\% \text{Fe}_2\text{O}_3$. The α grain size $\sim 1 \mu\text{m}$ for compositions $\leq 5\% \text{Fe}_2\text{O}_3$, and decreases to $\leq 200 \text{ nm}$ for compositions $\geq 10\% \text{Fe}_2\text{O}_3$ synthesized at 900°C , reflecting the strong effect of Fe_2O_3 on grain refinement relative to pure Al_2O_3 . The formation of single phase α in compositions $\leq 20\% \text{Fe}_2\text{O}_3$ appears to occur without the prior nucleation of Fe_2O_3 -rich "seeds", as suggested in the literature, whereas the partitioned α mixtures exhibit orientation relationships suggestive of epitaxial nucleation of one phase on the other. An enhanced understanding of the thermodynamics and transformation kinetics of this system emerges from the analysis of the present microstructures.

[†] A.D. Polli is Graduate Student Researcher in the Materials Department, University of California at Santa Barbara (UCSB); F.F. Lange is Professor of Materials and Chemical Engineering, and C.G. Levi is Professor of Materials and Mechanical Engineering at UCSB, Santa Barbara, CA 93106.

I. INTRODUCTION

Synthesizing ceramics from liquid precursors enables preparation of product forms not easily suited to traditional powder techniques. Alkoxides, nitrates, acetates, oxychlorides, and other solution chemistries may be spun into fibers or films and converted into oxides by pyrolysis,¹ usually at low to moderate temperatures in relation to their melting points. Alumina fibers produced in this manner are of significant commercial interest as reinforcements for metal- and ceramic-matrix composites.² The achievable strength (and to some extent the fracture toughness) of such fibers is known to be strongly influenced by grain size, which must be small relative to the fiber diameter in order to minimize the population of strength-limiting flaws.

When Al₂O₃ is prepared from precursor gels, pyrolysis usually yields first an amorphous material which must subsequently be converted to the stable corundum (α) form by heat treating. Nanocrystalline structures are readily achieved in many systems through devitrification of amorphous phases³ owing to the combination of large driving forces and constrained diffusion. However, controlling grain size in the pyrolytic synthesis of alumina is complicated by the evolution of metastable transitional phases between the amorphous and stable forms.⁴⁻⁷ While the specific phase sequence can vary with both the precursor and the heat treatment, the first crystallization product is often γ -Al₂O₃. This is a spinel-based structure with disordered cation vacancies which can order upon subsequent heating to yield δ or θ -Al₂O₃ prior to the evolution of α . Notwithstanding the higher driving force for crystallization of α -Al₂O₃, the evolution of an intermediate metastable γ form reduces the effective free energy available for nucleation of α grains. This in turn requires increased thermal activation (with transformation temperatures typically $\geq 900^\circ\text{C}$), which increases the α growth rate and promotes coarser grain sizes than those that might be possible upon direct crystallization.^{8,9}

Other sesquioxides with the corundum structure may exhibit either lower $\gamma \rightarrow \alpha$ transformation temperatures or suppression of the intermediate spinel phases. For example, synthesis of Fe₂O₃ by spray pyrolysis of nitrate solutions leads to the formation of γ -Fe₂O₃ below 500°C and subsequent conversion to α -Fe₂O₃ below ~600°C.¹⁰ Conversely, ligand field stabilization of the octahedral environment for Cr³⁺ in chromia forbids the formation of γ -Cr₂O₃, whereupon devitrification leads directly to the corundum structure.¹¹ These observations suggest that additions of Fe³⁺ and Cr³⁺ to Al₂O₃ precursor solutions may enhance the crystallization kinetics of alumina and promote the α -structure, both of which can lead to refined grain sizes.

Several authors have studied the effect of cation doping on the crystallization of alumina.¹²⁻¹⁵ Bye and Simpkin¹² investigated the effect of dilute Fe³⁺ doping on the $\gamma \rightarrow \alpha$ transition and showed that the conversion rate was substantially increased with only 2.5%Fe₂O₃.[§] It was postulated that the enhanced formation of α could arise from segregation of Fe₂O₃-rich clusters within the γ matrix which could nucleate α at much lower temperatures and act as "seeds" for the growth of α -Al₂O₃. This model was also used by Tsuchida et al.¹³ to explain similar results. McArdle and Messing^{16,17} showed that the $\gamma \rightarrow \alpha$ transition can indeed be promoted by adding ultrafine α -Fe₂O₃ crystals directly into alumina gels. The seeds obviate the need for nucleating α from γ and their number density and distribution essentially determines the final grain size. TEM studies have confirmed that α -Al₂O₃ does grow epitaxially from the α -Fe₂O₃ seeds.¹⁸

Phase relationships within the Al₂O₃-Fe₂O₃ system have been studied by several authors. The equilibrium diagram of Muan and Gee¹⁹, Figure 1, reveals the existence of a large miscibility gap between the oxides. Maximum solubilities of 25% Al₂O₃ in Fe₂O₃ and of 7% Fe₂O₃ in Al₂O₃ were estimated by Meyers et al.²⁰ The intermediate phase between ~1318-1410°C was determined by Dayal et al.²¹ to be orthorhombic (space-

§ All compositions in mole percent unless specified otherwise.

group Pc_{21n} , isomorphous with GaFeO_3 ²²) and is hereafter designated as $\text{O}-(\text{Al,Fe})_2\text{O}_3$. Recent convergent beam experiments on $\kappa\text{-Al}_2\text{O}_3$ have further revealed that the latter phase is also isomorphous with $\text{O}-(\text{Al,Fe})_2\text{O}_3$. The anions in these structures are arranged in close packed planes but stacked in an A-B-A-C sequence; distinctly different from either corundum or spinel. The phase field limits of $\text{O}-(\text{Al,Fe})_2\text{O}_3$ have been the subject of some debate,^{24,25} although it is generally agreed that its stability is confined within relatively small temperature and composition ranges. Synthesis of single phase $\text{O}-(\text{Al,Fe})_2\text{O}_3$ has been accomplished via liquid precursors,²⁶ but not by high temperature reaction of powders from the individual oxides.

This study was undertaken to enhance the understanding of the crystallization, phase transformation sequence and microstructure evolution mechanisms relevant to the control of grain size in the pyrolytic synthesis of alumina. The system selected is $\text{Al}_2\text{O}_3\text{-Fe}_2\text{O}_3$ but the compositions of interest (0 to 50% Fe_2O_3) extend well beyond the range of any other study reported in the literature. Particular emphasis is placed on the effects of Fe^{3+} additions on the relevant phase transformations.

II. EXPERIMENTAL PROCEDURES

Materials Synthesis

All materials were prepared using aqueous solutions of 0.35M $\text{Al}(\text{NO}_3)_3 \cdot 6\text{H}_2\text{O}$ and 0.5M $\text{Fe}(\text{NO}_3)_3 \cdot 6\text{H}_2\text{O}$ properly assayed to quantify their oxide yield. These were mixed to prepare solutions which would yield oxide mixtures with 0, 5, 10, 20, 30, 40, 50, and 100% Fe_2O_3 . Flash pyrolysis of the nitrate solutions was effected onto a Teflon-coated aluminum substrate held at 275°C, resulting in partially decomposed amorphous powders which were used as feedstock for subsequent heat treatments. Rapid drying promoted chemical homogeneity and prevented crystallization of the nitrates. The precursor powders were fully pyrolyzed into oxides by inserting the material directly

into a 25mm alumina tube furnace already at temperature (*upquenching*). Platinum crucibles were used to minimize any secondary reaction between the container and powder. Heat treatment conditions varied between 300 and 1100°C and from 2 min. to 24 h.

Thermal Analysis.

The transformation and decomposition behavior of the powders was examined by differential thermal analysis (DTA) and thermogravimetric analysis (TGA) using a General V4.1C DuPont 2000 analyzer. All experiments were performed with platinum crucibles. Phase transitions involving metastable materials are often very sluggish and can release heat over a large temperature range, making them more difficult to detect. Hence, DTA data were collected with heating rates of 25°C/min. in order to enhance the signal associated with phase transformations. TGA profiles were run at 10°C/min.

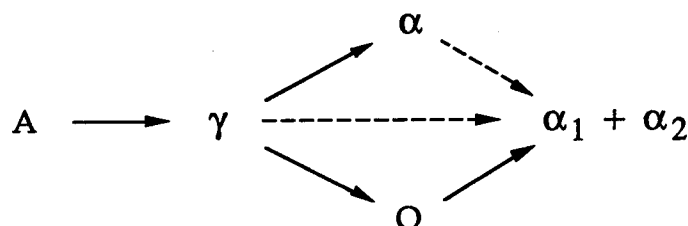
Chemical and Microstructural Analysis.

Bulk phase identification was performed by X-ray diffractometry (XRD) over the range $23^\circ < 2\theta < 70^\circ$ using a Scintag XDS 2000 diffractometer. Lattice parameters were determined from data collected with an internal silicon standard at 2θ speeds of 0.25°/minute. d-spacings for the (012), (104), (110), (113), (024), (116), (214), and (300) planes were fit with Pearson VII curves (PAD V Diffraction System, Scintag, Inc.) and used to refine the lattice parameters. Particles of the oxide powder were examined by transmission electron microscopy (TEM) using a JEOL 2000FX instrument operated at 200kV. For this purpose, the oxide powder was first suspended in ethanol and ground. A few drops of the suspension were subsequently placed onto a standard carbon film supported by a copper grid and allowed to dry, yielding sufficient thin area suitable for TEM observation. Selected area diffraction (SAD) and energy dispersive spectroscopy (EDS) (Link Analytical eXL) were used for microscopic phase identification and chemical composition, respectively. Camera lengths and K values were calibrated prior to the analysis to improve the accuracy of d-spacing and composition measurements.

III. RESULTS

General Trends

The DTA profiles for all compositions investigated showed either 2 or 3 exotherms, the first one corresponding to devitrification of the initial amorphous oxide and the subsequent one(s) to transformations of the metastable alumina form(s). XRD and TEM were used to elucidate the specific phase sequencing for each composition. The transformation paths identified can be summarized as follows:



The phase evolution map in Figure 2 depicts the onset temperatures observed for each transition under continuous heating at a rate of 25°C/min. The resulting "phase fields" reflect, albeit qualitatively, the effect of composition on the transformation kinetics and the relative stability of the different metastable phases. The "phase boundaries" in Figure 2 are obviously a function of the thermal history, becoming less defined and lower in temperature as the heating rate decreases. The extent of metastability induced by the low temperature processing may be inferred from comparison of Figures 2 and 1. The latter predicts only two equilibrium configurations for the system in the temperature-composition domain of Figure 2: α-(Al,Fe)₂O₃ as a single phase below 5-10%Fe₂O (shaded area in Figure 2), and mixed with α-(Fe,Al)₂O₃ at higher Fe³⁺ contents.

In general, all amorphous oxides crystallized to a single phase metastable spinel structure (γ), as detailed in the following section. Subsequent sections describe the rest of the transformation sequence, which varies with composition.

Devitrification of Precursor Powders.

All powders with compositions between 0 and 50% Fe_2O_3 were fully amorphous after completion of pyrolysis (marked by the drop of weight loss rate to negligible values in the TGA scans) and transformed to single phase $\gamma\text{-(Al,Fe)}_2\text{O}_3$ upon subsequent heating. Owing to the fine grain size of the γ phase, typically ~ 5 nm, and its weak scattering characteristics in XRD, it was necessary to use electron diffraction to ascertain conclusively the onset of crystallization. The problem was particularly evident in pure Fe_2O_3 , wherein no XRD peaks were resolvable after spray pyrolysis but TEM revealed that fine $\gamma\text{-Fe}_2\text{O}_3$ had already formed at this stage. (Decomposition of ferric nitrate appears to be completed at $\sim 250^\circ\text{C}$, below the spray pyrolysis temperature.)

The thermal activation required for the $\text{A} \rightarrow \gamma$ transition steadily decreased by $\sim 7^\circ\text{C}$ per % Fe_2O_3 addition in the range of 0 to 30%, as illustrated by Figure 2. One should emphasize, however, that the devitrification temperatures in Figure 2 are for a relatively high heating rate and hence that crystallization may be observed at lower temperatures under slower heating or isothermal treatments. For example, electron SAD revealed that γ nucleates from pure amorphous Al_2O_3 samples upquenched to 800°C for 4 minutes whereas DTA at $25^\circ\text{C}/\text{min}$ detects an onset temperature of $\sim 892^\circ\text{C}$ for the same transformation. Nevertheless, a clear correlation between Fe_2O_3 additions and devitrification temperature does seem to exist for any given thermal history.

Single Phase Microstructures (0 - 10% Fe_2O_3)

Compositions with 5 and 10% Fe_2O_3 followed the general transformation sequence established for pure Al_2O_3 , i.e. γ transformed to a single α phase which resisted further partitioning. (Ordering of γ prior to its transformation to α is quite possible but was not evident in the present experiments.) Figure 3 shows micrographs of Al_2O_3 with 0, 5 and 10% Fe_2O_3 upquenched at 900°C for 10 minutes. The pure Al_2O_3 and 5% Fe_2O_3 particles at this stage consist only of fine γ grains, Figures 3(a,b), with no evidence of α

detected by XRD. Comparison with the 10% Fe_2O_3 particle in Figure 3(c) shows the effect of a further addition of Fe^{3+} . Equiaxed α grains have nucleated and are growing from the γ matrix in the latter sample. The number density of α grains, which is essentially a manifestation of the nucleation frequency, is quite high. One might surmise that, if no more nuclei were to form, the resulting α grain size would be on the order of ~ 150 nm, consistent with the fully transformed microstructure after 1 h at 900°C , Figure 4(a). In contrast, the 5% Fe_2O_3 material processed in the same manner would be only partially transformed, with a final α grain size of ~ 1 μm .

According to the phase diagram in Figure 1, any single α phase composition above $\sim 7\%$ Fe_2O_3 should be metastable and would be expected to partition into two α structures, one Al_2O_3 -rich and the other Fe_2O_3 -rich. This was not observed in any of the 10% Fe_2O_3 specimens. XRD revealed that powders heat treated at 1100°C for as long as 2 h remained single phase α without evident change in composition, as inferred from the invariance of d-spacings. The evolution of an Fe_2O_3 -rich α is readily detected by the appearance of a second set of reflections with different spacings in both X-ray and electron diffraction, as noted below.

Two Phase Microstructures via α Partitioning (20 % Fe_2O_3)

The 20% Fe_2O_3 material followed initially the same transformation path as the 0-10% Fe_2O_3 powders, but underwent further partitioning into $\alpha_1 + \alpha_2$. Figure 3(d) shows the microstructure of this material upquenched at 900°C for 10 minutes. It is apparent from Figures 3(c,d) that doubling the Fe^{3+} concentration produces only a small increment in the number density of α nuclei under similar thermal histories. There is slightly more α in the 20% material, but the majority of the microstructure is still γ . The transformed microstructure after 1 h at 900°C is quite similar to that of 10% Fe_2O_3 , as shown in Figure 4, with a grain size on the order of ~ 150 nm. Extensive neck formation suggests that sintering and perhaps grain coarsening are already occurring at this stage.

XRD analysis of the sample in Figure 4(b) revealed only one set of α reflections rather than the two α phases anticipated from the phase diagram for compositions above $\sim 7\% \text{Fe}_2\text{O}_3$. Coupled with the previous results, this shows that the solubility of the single phase Al_2O_3 -rich α field can be extended at least up to $20\% \text{Fe}_2\text{O}_3$. Lattice parameters for α solid solutions between 0 and $20\% \text{Fe}_2\text{O}_3$ showed only a slight positive deviation from Vegard's law for a_0 , and a small negative deviation from linearity for c_0 . (The latter deviation disappeared by $\sim 20\% \text{Fe}_2\text{O}_3$). These results are similar to those found by other investigators.^{19,24} The near linearity in lattice parameters further suggests that the solid solutions were reasonably homogeneous.

Contrary to the $10\% \text{Fe}_2\text{O}_3$ material, which remained single phase for extended treatments at high temperature, the $20\% \text{Fe}_2\text{O}_3$ composition started partitioning after 1 h at 1000°C , albeit at a relatively sluggish rate. Even after 1 h at 1100°C the Al_2O_3 -rich phase had lattice parameters close to those of the initial $20\% \text{Fe}_2\text{O}_3$ single phase powder, suggesting that the bulk of the material had not changed significantly. Doublet spots were evident in the SAD patterns of the regions containing both α phases, suggesting some degree of epitaxy between them.

Compositions Forming an Intermediate Orthorhombic Phase ($\geq 30\% \text{Fe}_2\text{O}_3$)

An intermediate single phase α structure was not detected in any of the other compositions investigated (30 - $50\% \text{Fe}_2\text{O}_3$). In all cases the transformation of γ appeared to go into a mixture of two α phases either directly or through an intermediate metastable phase with orthorhombic structure.

Figure 5 shows XRD spectra for $30\% \text{Fe}_2\text{O}_3$ powders upquenched at temperatures of 800°C and 900°C for times ranging from 4 min. to 1 h. The specimen heated 4 min. at 800°C , Figure 5(a), shows only very diffuse γ peaks but TEM revealed a well developed nanocrystalline single phase γ structure. Conversely, two sets of α peaks are found after 4 min. at 900°C , Figure 5(b). Lattice parameter measurements suggest that one contains

~20% Fe₂O₃ and the other ~85% Fe₂O₃. Figure 6 shows the corresponding microstructure, consisting predominantly of α grains ~150 nm across. Small regions of γ remain, as in the region at the center of the micrograph denoted by arrows. The diffraction rings within the inset SAD pattern are found in pairs, as expected from the presence of two phases with the same structure (α) and different lattice parameters. Doublet spots suggestive of epitaxy were again evident in the combined SAD patterns of the α phases.

The diffraction peaks at 31.2°, 47.2°, and 63.0° in Figure 5(b) cannot be indexed to either the corundum (α) or the spinel (γ) structure. These correspond to O-(Al,Fe)₂O₃, as detailed in the subsequent analysis of the higher compositions. The relative proportion of O phase in the 30%Fe₂O₃ samples must be quite small as it was not detectable by TEM. Moreover, this phase vanishes from the XRD patterns of the 30% Fe₂O₃ powder after 1 h at 900°C, as noted in Figure 5(c) where all reflections can be indexed to the α structures.

The evidence of intermediate O phase formation was much stronger in the 40 and 50%Fe₂O₃ materials. Micrographs illustrating the progression of phases in the 40% sample after the initial devitrification to γ are shown in Figure 7. Only nanocrystalline γ was found by TEM for samples heated at 800°C for 4 minutes (not shown). XRD of the bulk powder showed traces of O-(Al,Fe)₂O₃ but no α at this stage, with traces of two α structures emerging only after 1 h at 800°C. However, TEM revealed that even after this longer treatment the material was mostly γ with small regions of O-(Al,Fe)₂O₃, one of which is shown in Figure 7(a). The O-(Al,Fe)₂O₃ grains in this micrograph may be identified by their streaky appearance. After 24 h at 800°C the O-(Al,Fe)₂O₃ peaks had nearly disappeared from the XRD patterns while both sets of α peaks became stronger. Figures 7(b-d) depict microstructural features of powders resulting from the latter treatment. The majority of the material consisted of a mixture of Al₂O₃-rich and Fe₂O₃-rich α grains, Figure 7(b), with an average size of ~200 nm. Epitaxy between α grains is evident from the doublet spots in the ring patterns. Most of the residual O-(Al,Fe)₂O₃

was found in small pockets surrounded by the α mixture, as illustrated in Figure 7(c), although larger clusters of O grains were found occasionally, as in Figure 7(d). EDS revealed average compositions of 39% Fe_2O_3 for the bulk particles in Figures 7(b-d) and 40% for the O phase, with individual grains of the latter ranging in composition from ~38 to ~44% (within the experimental scatter of the technique used). This suggests that bulk segregation is not a problem and also that partitioning is not significant until the final decomposition into the two corundum phases.

Micrographs illustrating the phase evolution of the 50% Fe_2O_3 powders are displayed in Figure 8. Single phase γ structures can still be retained by upquenching the precursor powder, as shown in Figure 8(a), but only at lower temperatures than those used in the leaner compositions, e.g. 700°C for 4 minutes. The micrographs in Figures 8(b,c) depict two particles from a sample upquenched at 800°C for 20 minutes, the first one showing equiaxed O grains growing within the γ , and the second one illustrating a fully transformed region. The mean grain size of O- $(\text{Al,Fe})_2\text{O}_3$ is ~100nm. The inset SAD patterns match the XRD data collected for the same powder.

The O phase appears in the above specimens at temperatures well below the lower stability limit (1318°C) predicted by the phase diagram in Figure 1. To confirm its identity, "equilibrium" O- AlFeO_3 was prepared by heating the 50% Fe_2O_3 amorphous powder at 1350°C for 4 minutes and rapidly cooling in air. Table 1 compares the ten most intense reflections from the JCPDS card with those in the XRD pattern of the material synthesized at 1350°C, and those determined by TEM of the sample pyrolyzed at 800°C for 24 h (the XRD of the latter are too diffuse to evaluate with confidence). Excellent agreement in d-spacings was found in all cases, with the relative intensities matching well for the 1350°C material, but not for that synthesized at 800°C. While this may be a consequence of the smaller sampling volume involved in the SAD analysis, it could also be a manifestation of disorder or other forms of structural imperfection. (The streaky appearance is indeed suggestive of stacking faults in the crystal.)

Only a small volume fraction of the O- $(\text{Al,Fe})_2\text{O}_3$ transforms to α after 24 h at 800°C. The two α phases consistently appeared mixed in colonies growing from the O phase, as illustrated in Figure 8(d). These colonies consist of several α grains of similar size but different compositions, as inferred from XRD analysis. As before, the presence of doublet spots in the SAD ring patterns suggested that the two α phases were epitaxially related.

A dark field analysis of the orientation relationships in the α colonies is presented in Figure 9. Figure 9(a) shows a magnified image of an α colony located in the lower right region of the micrograph in Figure 8(c). The corresponding diffraction pattern in Figure 9(b) indicates that the $[\bar{1}432]$ zone axis is aligned with the beam. The doublet spots indicative of epitaxy are now much more clearly defined than in the ring patterns. (The smaller spacings on the SAD pattern are associated with the Fe_2O_3 -rich phase and the larger ones with the Al_2O_3 -rich. The DF image in Figure 9(c) was generated using the doublet denoted by an arrow in Figure 9(b), whereas the image in Figure 9(d) arises from only the spot closer to the main beam. Careful examination of the images reveals that the colony contains three sets of α grains with sizes on the order of 150 nm. Average compositions of the two α structures based on EDS measurements on individual grains are ~11 and ~92% Fe_2O_3 . These values are close to those derived from lattice parameter measurements but somewhat higher than the equilibrium values anticipated from the phase diagram.

IV. DISCUSSION

Three dominant issues emerge from the previous results: (i) the consistent selection of metastable single phase $\gamma(\text{Al,Fe})_2\text{O}_3$ as the first product of crystallization, (ii) the synthesis of extended α and O solid solutions, and (iii) the partitioning behavior

of the extended solid solutions into two corundum structures. The effect of Fe₂O₃ content is clearly a key factor across the above transformations.

Phase Selection during Crystallization

The evolution of transitional spinel structures during pyrolysis of Al₂O₃ precursors is generally viewed as the underlying cause of the α -grain size control problem. From that perspective, it is important to understand the factors leading to the selection of spinel instead of the more stable corundum structure. The competition between these phases during crystallization of pure Al₂O₃ *from the melt* has been previously examined.²⁷ Even though α is always the thermodynamically favored phase, γ may be selected kinetically if there is a temperature wherein its energy barrier to nucleation becomes smaller than that of α . This critical temperature is approximately given by:

$$T_{\gamma/\alpha}^* = T_M^\alpha + (T_M^\alpha - T_M^\gamma) \left[1 - \frac{\Delta S_c^\alpha}{\Delta S_c^\gamma} \left(\frac{\sigma^\gamma \phi^\gamma}{\sigma^\alpha \phi^\alpha} \right)^{3/2} \right] \quad (1)$$

where T_M^n and ΔS_c^n are the melting temperature and volumetric entropy of crystallization for the competing phases (α or γ), respectively, σ^n is the corresponding liquid/solid interfacial energy, representing the barrier to the transformation, and ϕ^n is a factor accounting for the catalytic strength of the nucleation sites for each phase.²⁷ ($\phi = 1$ for homogeneous nucleation and diminishes as the potency of the site increases.) Using the thermochemical parameters in Table 2 and neglecting the effect of nucleation catalysts as a first approximation, one can show from Equation (1) that the phase selection may switch from α to γ below $\sim 1770^\circ\text{C}$, corresponding to a relatively modest undercooling of $\sim 0.12T_M^\alpha$. Selection of γ at lower undercoolings is still possible, but would require a stronger catalytic bias towards this phase, i.e. $\phi^\gamma < \phi^\alpha$.

In crystallization from an amorphous solid there is an additional barrier to nucleation arising from the elastic energy associated with the molar volume change.

The strain energy per unit volume of nucleus, ΔG_s^n , is given by Christian²⁸ for the case of a spherical particle as:

$$\Delta G_s^n = \frac{E_A E_n}{3(1-\nu_A)E_n + 6(1-2\nu_n)E_A} \left[1 - \frac{\Omega_A}{\Omega_n} \right]^2 \quad (2)$$

where E_i , ν_i and Ω_i are the elastic moduli, Poisson's ratio and molar volume of the amorphous (A) and nucleating (n) phases, respectively. The temperature at which the phase selection changes may now be redefined in terms of the modified nucleation barriers, ΔG_c^* , for the competing phases as

$$\frac{\Delta G_\gamma^*}{\Delta G_\alpha^*} = \left[\frac{\Delta S_c^\alpha (T_M^\alpha - T) + \Delta G_s^\alpha}{\Delta S_c^\gamma (T_M^\gamma - T) + \Delta G_s^\gamma} \right]^2 \left(\frac{\sigma^\gamma \phi^\gamma}{\sigma^\alpha \phi^\alpha} \right)^3 < 1 \quad (3)$$

where the product $\Delta S_c^n (T_M^n - T)$ is the chemical free energy change, ΔG_c^n , representing the driving force for the bulk transformation. Since $\Delta G_c < 0$ and $\Delta G_s > 0$, there will only be a net driving force for nucleation if

$$T < T_M^n + \frac{\Delta G_s^n}{\Delta S_c^n} \quad (4)$$

Using literature values for the molar volumes and the elastic properties of α -Al₂O₃, and estimates for γ from spinel structures (Table 2), one can calculate the strain energies for α and γ as ~ 1.30 and ~ 0.3 kJ/cm³, respectively. It may then be shown that the net driving force [$\Delta G_c + \Delta G_s$] is consistently larger for γ even though the chemical free energy, ΔG_c , is always greater for α .[§] (This does not imply that the bulk γ phase is more stable, but merely that it is less constrained from nucleating within the amorphous matrix.) Spinel nucleation from the amorphous phase becomes feasible at temperatures below $\sim 1770^\circ\text{C}$, whereas α requires temperatures below $\sim 1340^\circ\text{C}$ to develop a favorable net

§ This is relatively insensitive to the values of the elastic properties assumed for the spinel and amorphous phases as the relative strain energies are primarily controlled by the differences in molar volumes. The conclusion is still valid if $E_\gamma = E_\alpha$ and if $E_A > 100$ GPa.

driving force. (These values may change somewhat since temperature effects on the heat capacity, molar volumes and elastic properties were neglected, and also because strain energy effects may be relaxed by diffusional processes as $T \rightarrow T_M$. The kinetic hierarchy, however, is valid for all temperatures of interest in the present experiments.)

Owing to the sensitivity of the nucleation rate to the magnitude of ΔG^* , the elastic energy could have a much stronger effect than the interfacial energy on the competitiveness between α and γ . Assuming that the pre-exponential factors in the classical nucleation rate expression²⁸ are similar in magnitude for both phases, the calculated ratio of γ/α (homogeneous) nucleation rates for the temperatures of interest would be $<10^4$ if the strain rate contribution were neglected (as in crystallization from the melt), but $>10^{13}$ if it is included. The actual nucleation rate of spinel from the amorphous oxide is probably quite high, as manifested in the ultrafine grain size observed in the present experiments, as well as by devitrification of melt-quenched Al₂O₃ glass.²⁷

The present experiments show that metastable spinel formation appears to persist with Fe₂O₃ addition across the entire composition range, with a concomitant reduction in the devitrification temperature. The γ onset temperatures are $\sim 0.5T_M$ for Al₂O₃ and $\sim 0.3T_M$ for Fe₂O₃ (the latter assumes a melting point for α -Fe₂O₃ in the range $\sim 1500 \pm 100^\circ\text{C}$ from Figure 1). The reduced mobility expected at lower homologous temperatures suggests that the nucleation barrier is lower for pure Fe₂O₃, either because of an enhanced driving force or smaller interfacial/strain energy terms. Unfortunately, the lack of the requisite information on Fe oxides precludes quantification of this effect.

Comparison of calculated octahedral site preference energies (OSPE) for divalent and trivalent cations in binary spinels²⁹ could shed some light on the above issue. The OSPEs are approximately 16, -42 and -88 kJ/mole for Fe³⁺, Al³⁺, and Cr³⁺, respectively, where a more negative value represents a stronger preference for the octahedral sites. Prior studies^{7,30} have suggested that the stoichiometrically necessary cation vacancies in γ -Al₂O₃ are predominantly located in tetrahedral sites, in agreement with the strong

OSPE. Gradual substitution of Fe^{3+} for Al^{3+} in this defect spinel structure would be expected to promote a more random distribution of vacancies between octahedral and tetrahedral sites, potentially structural rearrangement that must take place during crystallization. In principle, this could translate into a reduction of the A/γ interfacial energy, and hence of the nucleation energy barrier, consistent with the observed reduction in the onset of the $\text{A} \rightarrow \gamma$ transformation. Conversely, the strongly negative OSPE of Cr^{3+} should preclude spinel formation in pure Cr_2O_3 . If Cr^{3+} were added to $\gamma\text{-Al}_2\text{O}_3$, however, it would be expected to replace initially the more abundant octahedral Al^{3+} , with no significant effect on the distribution of the charge-compensating vacancies. Indeed, work by the authors¹¹ has shown that spinel formation in $(\text{Al,Cr})_2\text{O}_3$ is not superseded until the concentration reaches $\sim 70\%\text{Cr}_2\text{O}_3$, whereupon the octahedral sites would be largely saturated and further addition of Cr^{3+} would have to occupy the more energetically unfavorable tetrahedral positions.

Partitionless Transformations of the Spinel

The phase evolution map in Figure 2 indicates that, with the exception of compositions in the vicinity of $30\%\text{Fe}_2\text{O}_3$, the γ produced by devitrification transforms into a single phase with either the corundum or orthorhombic structure prior to the final phase separation into $\alpha_1 + \alpha_2$. The transformation appears to be partitionless, with a change in phase selection from α to O at $\sim 30\%\text{Fe}_2\text{O}_3$. In conjunction with the phase diagram, this suggests that the relative positions of the free energy versus composition curves at the temperatures of interest are as depicted in Figure 10(a).

It has been shown elsewhere^{1,15} that if long range diffusion is constrained by the low (homologous) temperatures typical of precursor pyrolysis, the system tends to select during crystallization the phase which can provide the highest decrease in free energy without changing the composition. When there is a sequence of two or more partitionless transformations, as in the present case, the order of evolution reflects the

relative increase in kinetic hindrance.³¹ For example, for compositions between ~7 and ~20%Fe₂O₃ in Figure 10(a) the metastable α extended solution is clearly the one with the largest driving force, but γ forms first owing to its lower nucleation barrier, as in the pure Al₂O₃ case.

As the composition increases above ~20%Fe₂O₃ the selection is complicated by the introduction of the O phase in the thermodynamic menu, and by the appearance of the spinodal range in the miscibility gap. The O phase seems to have a substantial metastable homogeneity range, as it is detected at compositions as low as 30%Fe₂O₃, and should be more stable than the single α phase within the spinodal, even at temperatures below its equilibrium eutectoid decomposition into $\alpha_1 + \alpha_2$. This is suggested by the phase diagram and is consistent with the observed phase evolution sequence for the 40 and 50%Fe₂O₃ compositions. The relative positions of the α and γ free energy curves within the spinodal are less clear, but the formation of O-(Al,Fe)₂O₃ from γ —rather than the less crystallographically complex α —as a precursor to the partitioned $\alpha_1 + \alpha_2$ mixture suggests that $\Delta G_c^\alpha > \Delta G_c^\gamma$ in the 40-50% range. (It is also possible that α has a lower free energy than γ , but the difference in free energies may not be sufficiently large to overcome the kinetic hindrance.) The much faster and apparently direct partitioning of 30%Fe₂O₃ γ into $\alpha_1 + \alpha_2$, coupled with the simultaneous observation of traces of the O phase, suggest the availability of two competitive transformation paths involving the formation of metastable single phase O and α phases. The latter, however, would be within the spinodal range and thus likely to partition readily into $\alpha_1 + \alpha_2$.

The kinetic hindrance to the $\gamma \rightarrow \alpha$ transformation, essentially responsible for the exacerbated α grain growth in pure Al₂O₃, appears to persist throughout the range investigated, as revealed by the need for significant thermal activation above the devitrification temperature. Nevertheless, all compositions between 10 and 50%Fe₂O₃ show consistently fine grain sizes, ≤ 200 nm, suggesting a saturation in the marked grain refining effect of Fe₂O₃ clearly evident at concentrations below ~10%.

The grain refining mechanism in Fe₂O₃-doped Al₂O₃ has been the subject of previous studies.¹²⁻¹⁸ The prevailing view ascribes the refinement to the precipitation of numerous Fe₂O₃-rich (presumably α_2) seeds from γ , which subsequently act as heterogeneous nucleation sites for the bulk Al₂O₃-rich α_1 .^{12,13} No evidence was found to confirm this "seeding" effect; both X-ray and electron diffraction revealed only one α structure resulting from the transformation of γ for compositions $\leq 20\%$ Fe₂O₃ even after prolonged heating at 900°C, while EDS analysis gave no indication of detectable solute segregation in the scale of the grain size. Indeed, one might argue that if diffusion were sufficiently active to enable the formation of Fe₂O₃-rich α_2 seeds, the growth of α_1 from γ might not be partitionless and the resulting structure should contain both corundum phases. Conversely, it is possible that Fe/Al concentration gradients may develop within the Al-rich α_1 grains, as suggested by Figure 10(b). Assuming that the curvatures of the γ and α free energy curves are as shown in Figure 10(a)[§], there should be a composition on the Al-rich side wherein the tangents to the α and γ curves are equal, as illustrated in Figure 10(b), and hence where the driving force for the transformation will be maximized. This critical composition, C^* , is probably under the solubility limit of the single phase α_1 field, i.e. between 5 and 10% Fe₂O₃ for the temperatures of interest.

If some diffusion were allowed during the transformation, an initial γ composition below C^* could experience a higher reduction in free energy if it nucleated α slightly enriched in Fe, rather than with the same chemistry as the parent γ . (The Fe enrichment may further promote nucleation by reducing the strain energy barrier, given that the molar volume of α increases with Fe content.) Once nucleation occurs, growth can readily continue on the initial α , notwithstanding the gradual increase in the Al content anticipated from the requirement for solute conservation, and the concomitant reduction in driving force. (Note that the latter should not decrease below that of pure

[§] The different shapes are suggested by the presence of a miscibility gap in the corundum phase and the absence of any observed partitioning in γ , even at compositions as high as 50% Fe₂O₃.

Al₂O₃, and it is well established that in that limit growth is still much more active than nucleation at any given temperature.) From a rigorous viewpoint, this mechanism does not involve seeding as no need for renucleation is implied. Increasing Fe concentration in the range below C* should result in a higher Fe content for the first α , hence an enhanced driving force and perhaps a reduced nucleation barrier. As the Fe content approaches C* the need for solute redistribution to enhance the driving force decreases, and so does the requisite diffusion with a concomitant kinetic benefit. An interesting corollary to this scenario is that compositions above C* would tend to form Al-rich α upon nucleation. It appears, however, that the rate is not greatly affected, as noted by the similar density of α grains for 10 and 20%Fe₂O₃ in Figures 3 and 4.

Final Partitioning into $\alpha_1 + \alpha_2$

With the possible exception of the 10%Fe₂O₃ material, all compositions within the equilibrium two phase field eventually partitioned into $\alpha_1 + \alpha_2$, regardless of the intermediate phase. The resistance to partitioning of the 10%Fe₂O₃ supersaturated α , relative to the similar microstructure with 20%Fe₂O₃, is consistent with the smaller difference in free energy expected between the extended solid solution and the equilibrium $\alpha_1 + \alpha_2$ mixture, as illustrated by Figure 10(a). Partitioning is clearly promoted by increasing temperature, partially relieving the diffusional constraint, but the effect is counteracted by a reduction in the driving force resulting from the increasing solubility of Fe₂O₃ in α_1 . Precipitation of α_2 is nonetheless dictated by thermodynamics, presumably requiring longer times than those used in the present experiments.

The consistent observation of epitaxial relationships between the two α phases in the partitioned structures suggests two possible mechanisms for phase separation: spinodal decomposition or nucleation of one α phase on the other. While spinodal decomposition cannot be completely ruled out in the transitional 30% composition, it is clearly not an option for the $O \rightarrow \alpha_1 + \alpha_2$ transformation in the 40-50%Fe₂O₃ range, as inferred

from the relative shape and positions of the O and α free energy curves. Conversely, TEM analysis of the 20%Fe₂O₃ composition soon after the onset of phase separation reveals only a few α_2 crystals with grain sizes comparable to the parent α structure and spaced in a scale much larger than the original α grain size. This is difficult to reconcile with spinodal decomposition, but it is perfectly consistent with nucleation (presumably at grain boundaries) and epitaxial growth of α_2 on one of the neighboring α_1 crystals.

The observation of clusters of epitaxially related grain pairs with sizes comparable or larger than the original O phase in the 40-50% compositions suggests the following sequence of events. The α phase with the larger driving force (clearly the Al-rich α_1 for the 40% Fe₂O₃ material, as inferred from Figure 10, and perhaps also for 50%) is likely to nucleate first at O grain boundaries. Growth of the α_1 nucleus would reject Fe³⁺ in its vicinity, promoting nucleation of the α_2 phase on the initial α_1 , which is a more favorable site than the surrounding O matrix. Subsequent growth of α_2 depletes Fe³⁺ from its surroundings, promoting nucleation of a second α_1 grain which again is more favorable on the existing α_2 . In principle, each colony could grow from a single α_1 nucleation event, since the alternating α_2/α_1 nucleation process is more efficient than the α_1/O . The colony spacing is then a reflection of the number density of $O \rightarrow \alpha_1$ events, whereas the grain size within the colony results from the relative activity of the α_2/α_1 nucleation and growth processes. The presence of more than one family of orientations within each colony indicates that secondary α_1/O events occasionally occur at the periphery of the growing colony. This can be ascribed to the local solute supersaturation associated with the α_2/α_1 growth process, which induces a higher probability for an α grain to nucleate near the colony than away from it.

The 30%Fe₂O₃ composition exhibited substantially faster partitioning and somewhat finer grain size than the rest of the materials in the two phase range, with most of the $\alpha_1 + \alpha_2$ grains found as individual pairs, rather than colonies. This suggest that most of the $\alpha_1 + \alpha_2$ mixture evolves directly from γ , rather than through an intermediate

O phase stage. In light of the discussion above, one may hypothesize that the finer structure and more random distribution of orientations suggest that nucleation of α_1 from γ is more competitive at this composition than that from the O phase at the higher Fe contents. This would be consistent with the much higher density of grain boundary area in the parent γ , although the details are still unclear. There is also the possibility that metastable $\alpha_{(1)}$ forms from γ and then precipitates α_2 by spinodal decomposition. However, the comparable grain sizes of the α phases would then imply substantial coarsening of α_2 after precipitation, which is questionable in the time scale of the transformation for this particular composition (4 min at 900°C).

V. CONCLUSIONS

It has been shown that additions of Fe^{3+} have significant effects on the crystallization behavior and microstructural development of Al_2O_3 from liquid precursors. Several transformation paths were identified in the 0-50% Fe_2O_3 range, all starting with the formation of an amorphous oxide which devitrifies to a single phase spinel structure, and all culminating with the formation of one or two corundum phases depending on the corresponding equilibrium configuration. The γ may transform directly into $\alpha_1 + \alpha_2$ or, more commonly, via an intermediate extended solid solution with the corundum or orthorhombic- AlFeO_3 structures (above and below 30% Fe_2O_3 , respectively). Increases in Fe_2O_3 content from 0 to 50% enhance the initial nucleation of γ from the amorphous phase, as well as its subsequent transformation into α or O. The final decomposition into α_1 and α_2 is fastest at 30% Fe_2O_3 , when it appears to occur directly from the metastable γ , but is gradually hindered by Fe_2O_3 additions when it involves a transitional O phase, and by Al_2O_3 additions when the intermediate phase is the extended α solid solution.

The latter stages in the transformation path appear to be controlled primarily by the driving force, whereas the formation of metastable spinel and extended α and O solid solutions are clearly a consequence of the constraints to nucleation and solute redistribution. It appears that the strain energy associated with the nucleation process is a determinant factor in the kinetic selection of γ over α . The formation of intermediate phases essentially reduces the driving force available for the nucleation of α , reducing the number density of grains and hence producing a coarser structure than that in the original γ .

Fe additions to the precursor have a marked effect on the α grain size, reducing it from $\sim 1\ \mu\text{m}$ for compositions $\leq 5\%\text{Fe}_2\text{O}_3$ to $\sim 200\ \text{nm}$ for $\geq 10\%\text{Fe}_2\text{O}_3$. The final grain size for the single phase compositions is essentially a consequence of the effects of Fe on the driving force, and possibly on the strain and interfacial energies. While no evidence of "seeding" by initial precipitation of Fe-rich α crystals was found, a mechanism was outlined wherein local redistribution of Fe could enhance the direct nucleation of Al-rich α . The grain size evolution for compositions involving two α phases is a more complex process presumably involving nucleation of α_1 from the supersaturated α , γ or O transitional phases, and subsequent nucleation and epitaxial growth of the Fe-rich α_2 on the α_1 crystals. The evolution of $\alpha_1 + \alpha_2$ colonies was ascribed to the relative competition between the α_1/O and α_1/α_2 nucleation processes.

ACKNOWLEDGEMENTS

This investigation was sponsored by the Office of Naval Research under Contract N00014-92-J-1991, monitored by Dr. S.G. Fishman, and by the Air Force Office of Scientific Research under AASERT Grant F49620-93-1-0358DEF, monitored by Dr. A. Pechinek. The authors are grateful to Dr. D. Wilson of 3M Center in Minneapolis, MN, for introducing them to this problem and for useful discussions.

REFERENCES.

1. F.F. Lange, "Liquid Precursors for Ceramics: Kinetically Limited Crystallization, Spherical Particles, Fibers, and Thin Films", pp. 611-26 in *Chemical Processing of Advanced Materials*. eds. L.L. Herch and J.K. West. John Wiley and Sons, Inc. (1992).
2. A. G. Evans, "Perspective on the Development of High-Toughness Ceramics," *J. Am. Ceram. Soc.*, **73** [2] 187-206 (1990).
3. A. Rousset, F. Chassagneux, and J. Paris, "Preparation and Properties of Active Submicronic Solids and New Metastable Phases Obtained via a Metal-Organic Precursor Method," *J. Mater. Sci.*, **21** [9] 3111-5 (1986).
4. H. C. Stumpf, A. S. Russel, J. W. Newsome, and C. M. Tucker, "Thermal Transformations of Alumina and Alumina Hydrates," *Ind. Eng. Chem.*, **42** [3] 1398-403 (1950).
5. B. C. Lippens and J. H. deBoer, "Study of Phase Transformations During Calcination of Aluminum Hydroxides by Selected Area Diffraction," *Acta. Cryst.*, **17** 1312-21 (1964).
6. S. J. Wilson, "The Dehydration of Boehmite, $\gamma\text{-AlOOH}$, to $\gamma\text{-Al}_2\text{O}_3$," *J. Solid State Chem.*, **30** 247-55 (1979).
7. V. Jayaram and C. C. Levi, "The Structure of δ -Alumina Evolved from the Melt and the $\gamma \rightarrow \delta$ Transformation," *Acta. Metall.* **13** [2] 569-78 (1989).
8. K.J. Morrissey, K. K. Czanderna, and C. B. Carter, "Growth of $\alpha\text{-Al}_2\text{O}_3$ Within a Transition Alumina Matrix," *J. Am. Ceram. Soc.*, **66** [5] C88-90 (1984).
9. T. C. Chou and T. G. Nieh, "Nucleation and Concurrent Anomalous Grain Growth of $\alpha\text{-Al}_2\text{O}_3$ During $\gamma \rightarrow \alpha$ Phase Transformation," *J. Am. Ceram. Soc.*, **74** [9] 2270-79 (1991).
10. T. González-Carreño, M.P. Morales, M. Gracia, and C.J. Serna, "Preparation of Uniform $\gamma\text{-Fe}_2\text{O}_3$ Particles with Nanometer Size by Spray Pyrolysis," *Mat. Lett.*, **18** 151-5 (1993).
11. A. D. Polli, F. F. Lange, and C. G. Levi, unpublished work.
12. G. C. Bye and G. T. Simpkin, "Influence of Cr and Fe Formation of $\alpha\text{-Al}_2\text{O}_3$ from $\gamma\text{-Al}_2\text{O}_3$," *J. Am. Ceram. Soc.*, **57** [8] 367-71 (1974).
13. T. Tsuchida, R. Furuichi, T. Ishii, and K. Itoh, "The Effect of Cr^{3+} and Fe^{3+} Ions on the Transformation of Different Aluminum Hydroxides to $\alpha\text{-Al}_2\text{O}_3$," *Thermochimica Acta.*, **64** 337-53 (1983).
14. L.A. Xue and I. W. Chen, "Influence of Additives on the γ -to- α Transformation of Alumina," *J. Mater. Sci. Lett.*, **11** 443-5 (1992).
15. M.L. Balmer, F. F. Lange, and C. G. Levi, "Metastable Phase Selection and Partitioning for $\text{Zr}_{(1-x)}\text{Al}_x\text{O}_{(2-x/2)}$ Materials Synthesized with Liquid Precursors," *J. Am. Ceram. Soc.* **77** [8] 2069-75 (1994).
16. J.L. McArdle and G.L. Messing, "Transformation and Microstructural Control in Boehmite-Derived Alumina by Ferric Oxide Seeding," *Adv. Ceram. Mater.*, **3** 387-92 (1988).
17. J.L. McArdle and G. L. Messing, "Transformation, Microstructure Development, and Densification in $\alpha\text{-Fe}_2\text{O}_3$ -Seeded Boehmite-Derived Alumina," *J. Am. Ceram. Soc.*, **76** [1] 214-22 (1993).

18. J. L. McArdle, G. L. Messing, L. A. Tietz, and C. B. Carter, "Solid-Phase Epitaxy of Boehmite-Derived α -Alumina on Hematite Seed Crystals," *J. Am. Ceram. Soc.*, **72** [5] 864-67 (1989).
19. A. Muan and C. L. Gee, "Phase Equilibrium Studies in the System Iron Oxide - Al₂O₃ in Air and at 1 Atm. Pressure," *J. Am. Ceram. Soc.*, **39** [6] 207-14 (1956).
20. C.E. Meyers, T.O. Mason, W.T. Petuskey, J.W. Halloran, and H.K. Bowen, "Phase Equilibria in the System Fe-Al-O," *J. Am. Ceram. Soc.*, **63** [11-12] 659-63 (1980).
21. R.R. Dayal, J. A. Gard, and F. P. Glasser, "Crystal Data on FeAlO₃," *Acta. Cryst.*, **18** 574-5 (1965).
22. S. C. Abrahams, J. M. Reddy, and J. L. Bernstein, "Crystal Structure of Piezoelectric Ferromagnetic Gallium Iron Oxide," *J. Chem. Phys.*, **42** [11] 3957-68 (1965).
23. P. Liu and J. Skogsmo, "Space-Group Determination and Structure Model for κ -Al₂O₃ by Convergent-Beam Electron Diffraction," *Acta. Cryst.*, **B47** 425-33 (1991).
24. L. M. Altas and W. K. Sumida, "Solidus, Subsolidus and Subdissociation Phase Equilibria in the System Fe-Al-O," *J. Am. Ceram. Soc.*, **41** [5] 150-60 (1958).
25. A. Muan, "On the Stability of the Phase Fe₂O₃·Al₂O₃," *Am. J. Sci.*, **256** 413-22 (1958).
26. X. Devaux, A. Rousset, M. Broto, H. Rakoto, and S. Askenazy, "FeAlO₃: New Production Methods and Study of its Magnetization in very High Intensity Pulsed Magnetic Fields," *J. Mater. Sci. Lett.*, **9** 371-2 (1990).
27. C.G. Levi, V. Jayaram, J.J. Valencia, and R. Mehrabian, "Phase Selection in Electrohydrodynamic Atomization of Alumina," *J. Mater. Res.*, **3** [5] 969-83 (1988).
28. J.W. Christian, *The Theory of Transformations in Metals and Alloys*, 2nd ed., Part I, Ch. 10, Pergamon Press, Oxford, (1975).
29. A. Navrotsky and O.J. Kleppa, "The Thermodynamics of Cation Distributions in Simple Spinel," *J. Inorg. Nucl. Chem.*, **29** 2701-14 (1967).
30. L. Bragg, G.F. Claringbull, and W.H. Taylor, "Crystal Structures of Minerals", Cornell University Press, Ithaca, NY (1965).
31. V. Jayaram, M. De Graef and C.G. Levi, "Metastable Extension of the Fluorite Phase Field in Y₂O₃-ZrO₂ and its Effect on Grain Growth," *Acta Metall. Mater.*, **42**(6) 1829-1846 (1994).

Table 1. Comparison of interplanar spacings corresponding to the strongest reflections for O-AlFeO₃ from JCPDS file and 50%Fe₂O₃ material synthesized from liquid precursors at two temperatures.

O-Plane	Spacing (pm)		
	JCPDS	XRD (1350°C)	TEM (800°C)
(220)	314.6	313.9	313
(130)	290.0	289.3	288
(221)	265.8	265.3	267
(131)	250.6	249.3	
(311)	239.4	240.2	240
(321)	218.5	218.0	218
(331)	193.1	192.8	193
(341)	169.2	168.7	169
(351)	148.3	148.0	148
(303)	143.7	143.5	144

Table 2. Constants use in evaluating the driving force and energy barrier for Al₂O₃ nucleation.*

Property	α -Al ₂ O ₃	γ -Al ₂ O ₃	A-Al ₂ O ₃
Melting Temperature (K)	2327	2289	
Volumetric enthalpy of melting (kJ/cm ³)	4.35	2.82	
Interfacial energy (mJ/m ²)	450	310	
Molar volume (cm ³ /mole)	25.57	27.85	30.69
Young's modulus (GPa)	390	240	100
Strain energy for crystallization (kJ/cm ³)	1.33	0.30	

* Mechanical properties for γ -Al₂O₃ where estimated with those of spinel.

LIST OF FIGURE CAPTIONS.

- Figure 1. Phase diagram for the Al_2O_3 - Fe_2O_3 system according to Muan and Gee.¹⁹ This is not a true binary diagram; the presence of an equilibrium spinel form for pure Fe_2O_3 above $\sim 1380^\circ\text{C}$ suggests partial reduction of the latter to FeO at the higher temperatures.
- Figure 2. Phase evolution map for the Al_2O_3 - Fe_2O_3 system. The lines correspond to the onset of evolution of the phase immediately above under DTA at $25^\circ\text{C}/\text{min}$. The nature of the evolving structures was determined by XRD and/or TEM. The shaded area on the pure Al_2O_3 side represents the equilibrium α_1 field.
- Figure 3. TEM micrographs of Al_2O_3 powders with (a) 0, (b) 5, (c) 10, and (d) 20% Fe_2O_3 produced by upquenched amorphous precursor at 900°C for 10 minutes. The fine background is γ in all cases, with the larger crystallites in (c,d) corresponding to evolving α grains.
- Figure 4. TEM micrographs of (a) 10 and (b) 20% Fe_2O_3 compositions upquenched at 900°C for 1 h. Each sample consists of single phase α grains.
- Figure 5. XRD patterns from 30% Fe_2O_3 powders upquenched at (a) 800°C for 4 minutes, (b) 900°C for 4 minutes, and (c) 900°C for 1 h. The profiles show both the emergence of $\text{O}-(\text{Al,Fe})_2\text{O}_3$, α_1 and α_2 in (b) and the subsequent elimination of O in (c).
- Figure 6. TEM micrograph of 30% Fe_2O_3 powder upquenched at 900°C for 4 minutes. The bulk of the microstructure is $\alpha_1 + \alpha_2$. Arrows denote small regions of residual γ .
- Figure 7. TEM micrographs of 40% Fe_2O_3 powders upquenched at (a) 800°C for 1 h and (b-d) 800°C for 24 h. Fine grain γ gives way to $\text{O}-(\text{Al,Fe})_2\text{O}_3$ and eventually to $\alpha_1 + \alpha_2$.
- Figure 8. TEM micrographs of 50% Fe_2O_3 powder upquenched at (a) 700°C for 4 min., (b,c) 800°C for 20 min., and (d) 800°C for 24 h. $\alpha_1 + \alpha_2$ evolve from $\text{O}-(\text{Al,Fe})_2\text{O}_3$ only for the longest treatment.
- Figure 9. Dark field (DF) analysis of an α colony within the 50% Fe_2O_3 material. Micrographs show (a) a bright field image of an α colony, (b) the $[\bar{1}432]$ zone axis diffraction pattern from the colony, (c) DF image using both spots indicated by arrow in (b), and (d) DF image from the spot closest to the central beam.
- Figure 10. Schematic free energy diagram for the Al_2O_3 - Fe_2O_3 system in the temperature range investigated. Arrows in (a) represent free energy changes corresponding to the observed transformation sequences. (b) depicts the composition ranges in which Fe or Al enrichment are favored during nucleation when limited diffusion is allowed.

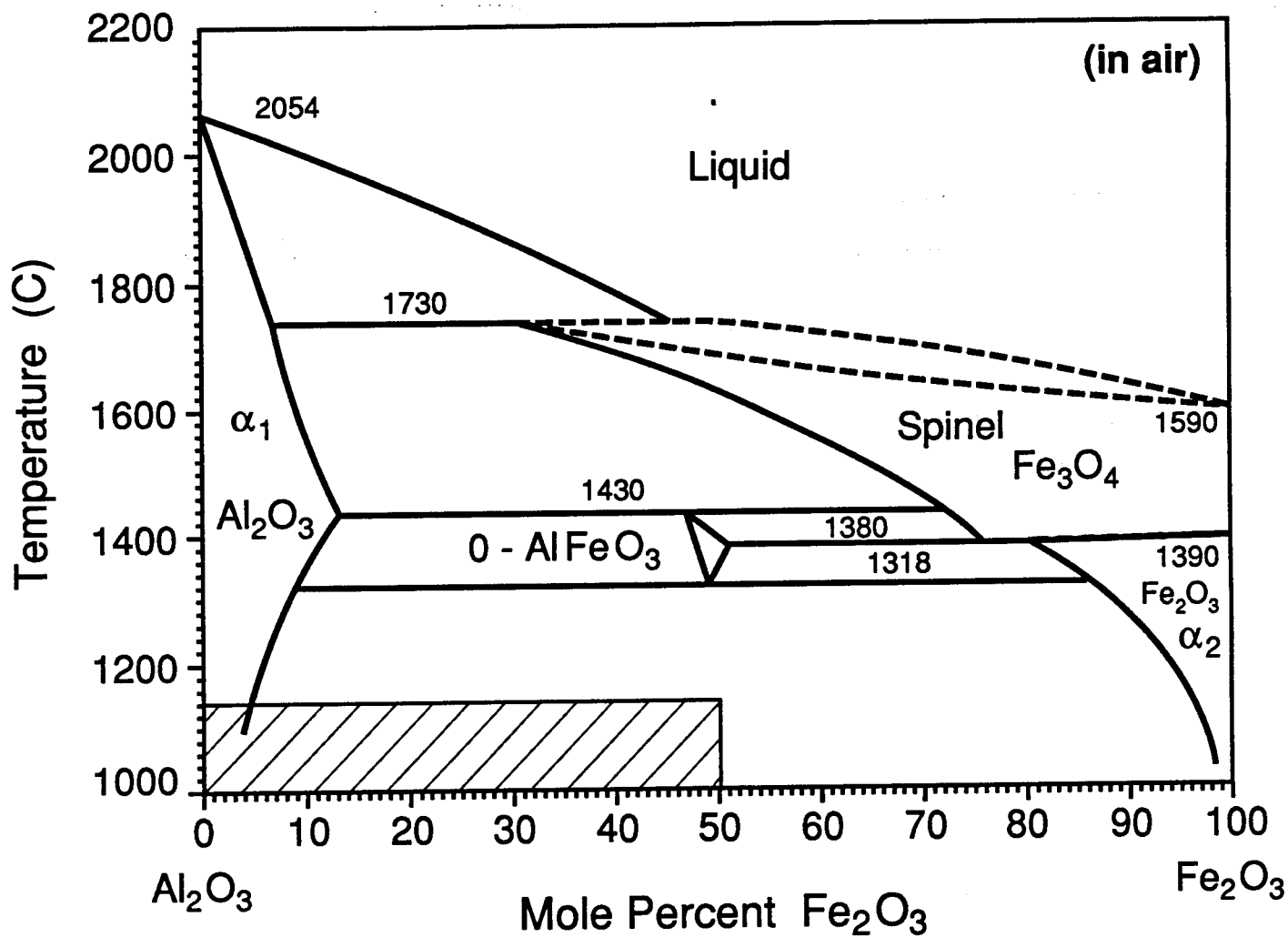


Figure 1. Phase diagram for the Al_2O_3 - Fe_2O_3 system according to Muan and Gee.¹⁹ This is not a true binary diagram; the presence of an equilibrium spinel form for pure Fe_2O_3 above $\sim 1380^\circ\text{C}$ suggests partial reduction of the latter to FeO at the higher temperatures.

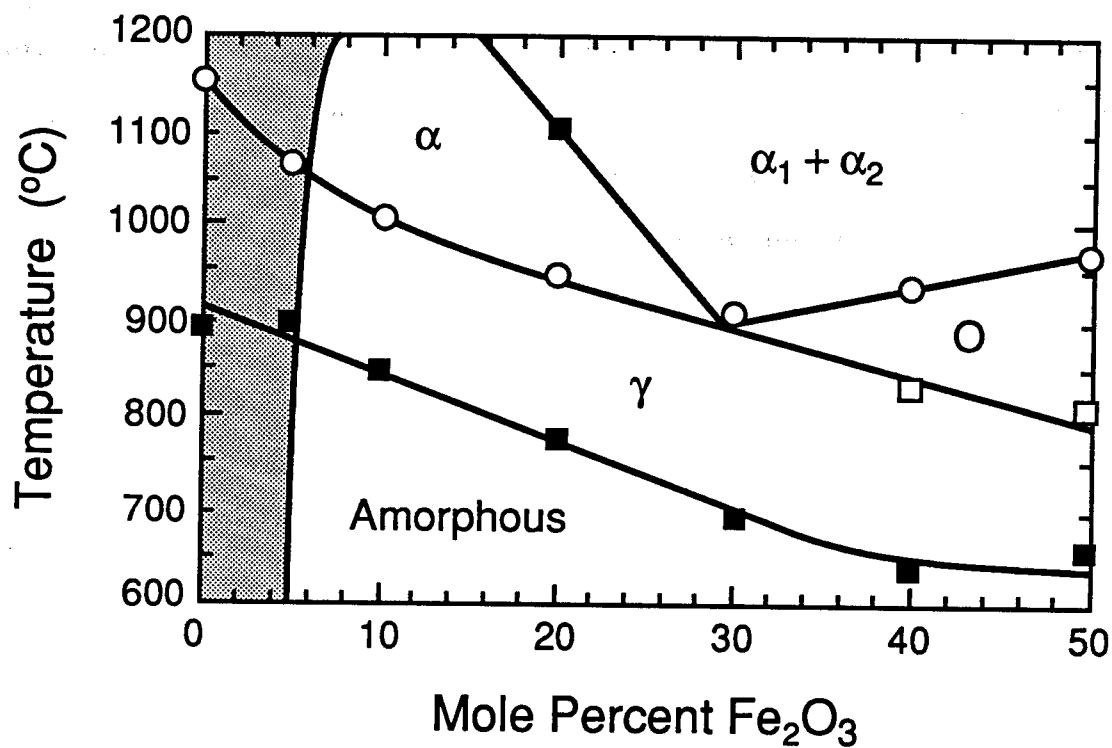


Figure 2. Phase evolution map for the Al_2O_3 - Fe_2O_3 system. The lines correspond to the onset of evolution of the phase immediately above under DTA at $25^{\circ}\text{C}/\text{min}$. The nature of the evolving structures was determined by XRD and/or TEM. The shaded area on the pure Al_2O_3 side represents the equilibrium α_1 field.

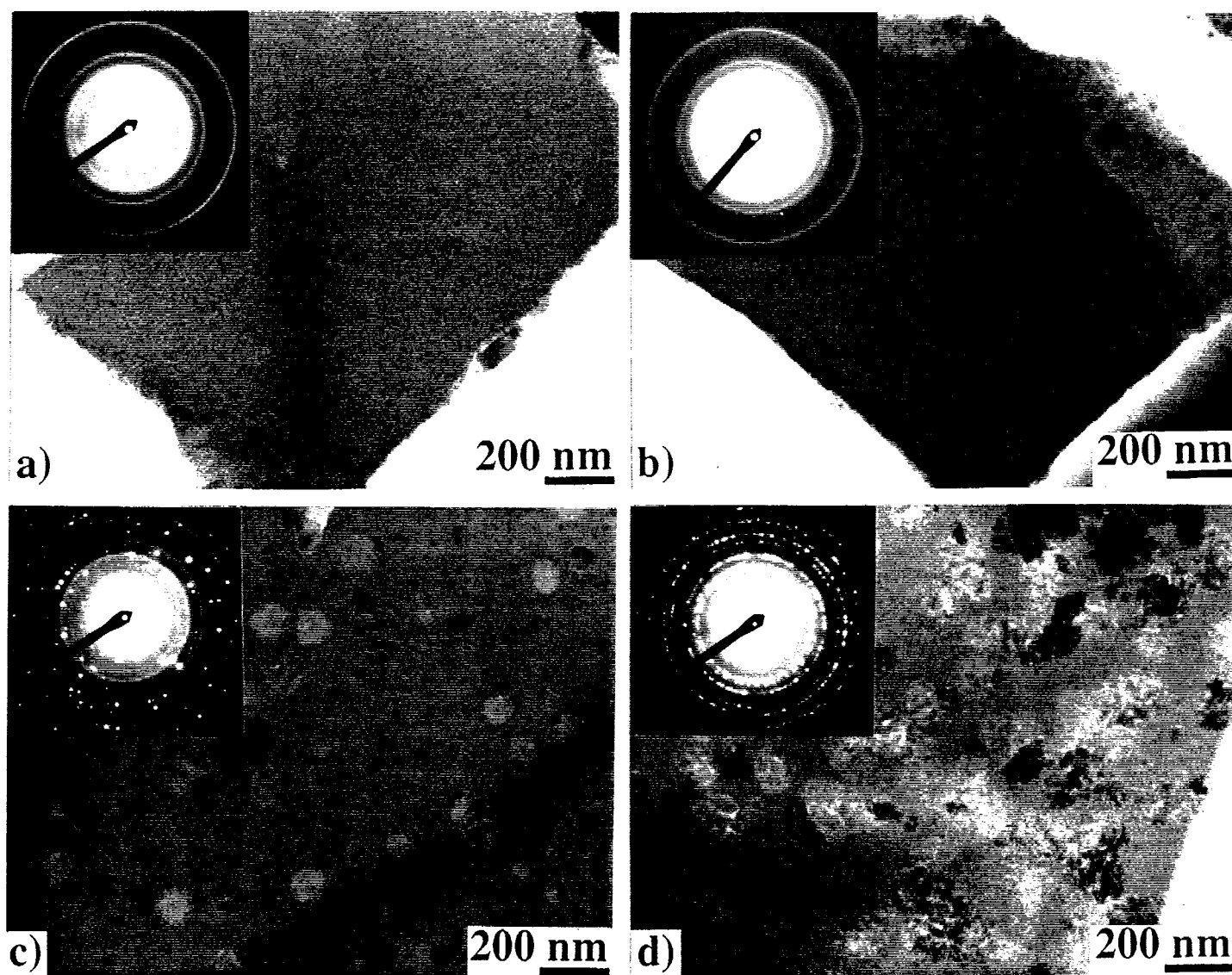


Figure 3. TEM micrographs of Al_2O_3 powders with (a) 0, (b) 5, (c) 10, and (d) 20% Fe_2O_3 produced by upquenched amorphous precursor at 900°C for 10 minutes. The fine background is γ in all cases, with the larger crystallites in (c,d) corresponding to evolving α grains.

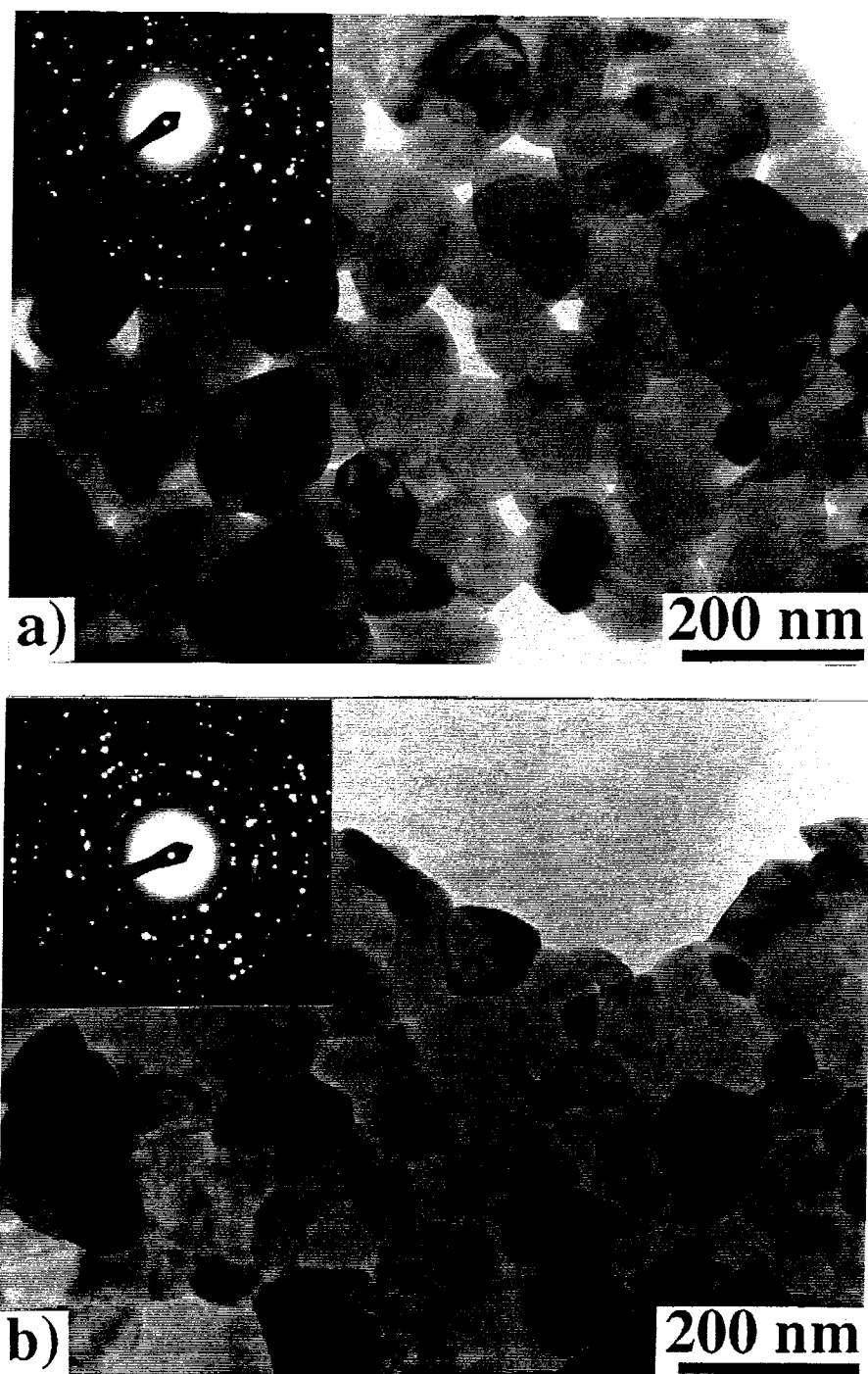


Figure 4. TEM micrographs of (a) 10 and (b) 20% Fe_2O_3 compositions upquenched at 900°C for 1 h. Each sample consists of single phase α grains.

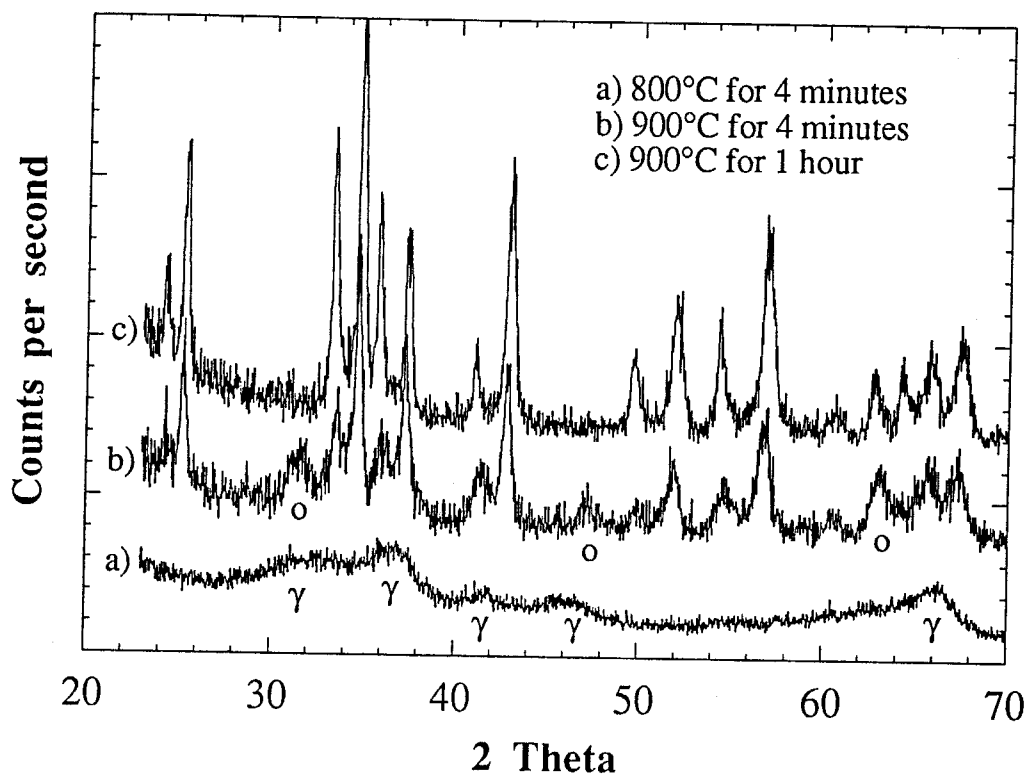


Figure 5. XRD patterns from 30% Fe_2O_3 powders upquenched at (a) 800°C for 4 minutes, (b) 900°C for 4 minutes, and (c) 900°C for 1 h. The profiles show both the emergence of $\text{O}-(\text{Al,Fe})_2\text{O}_3$, α_1 and α_2 in (b) and the subsequent elimination of O in (c).

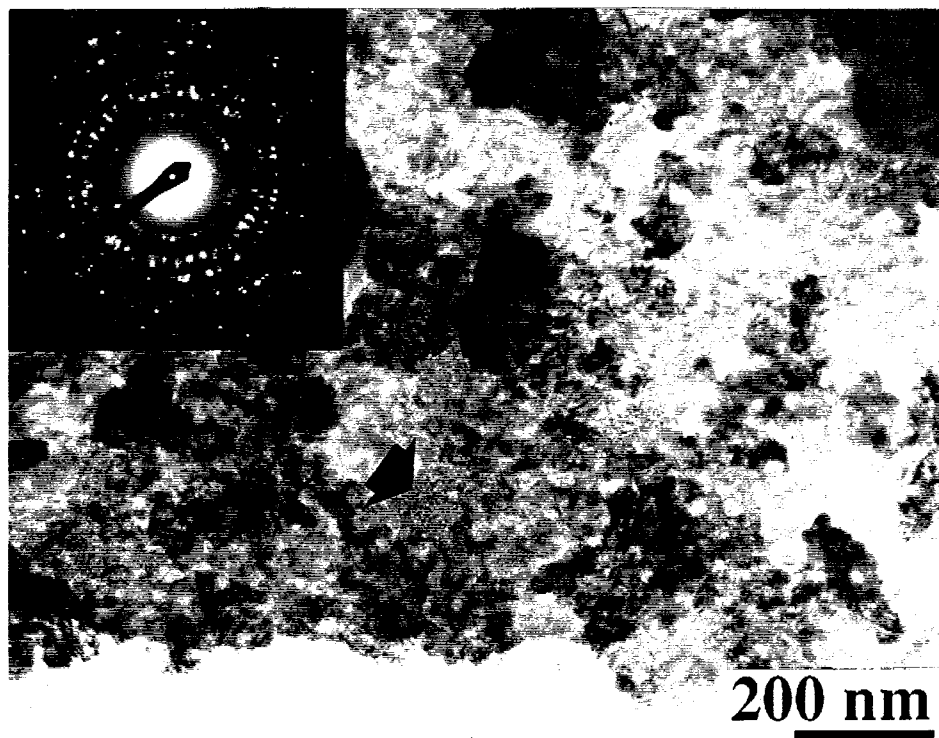


Figure 6. TEM micrograph of 30% Fe₂O₃ powder upquenched at 900 for 4 minutes. The bulk of the microstructure is $\alpha_1 + \alpha_2$. Arrows denote small regions of residual γ .

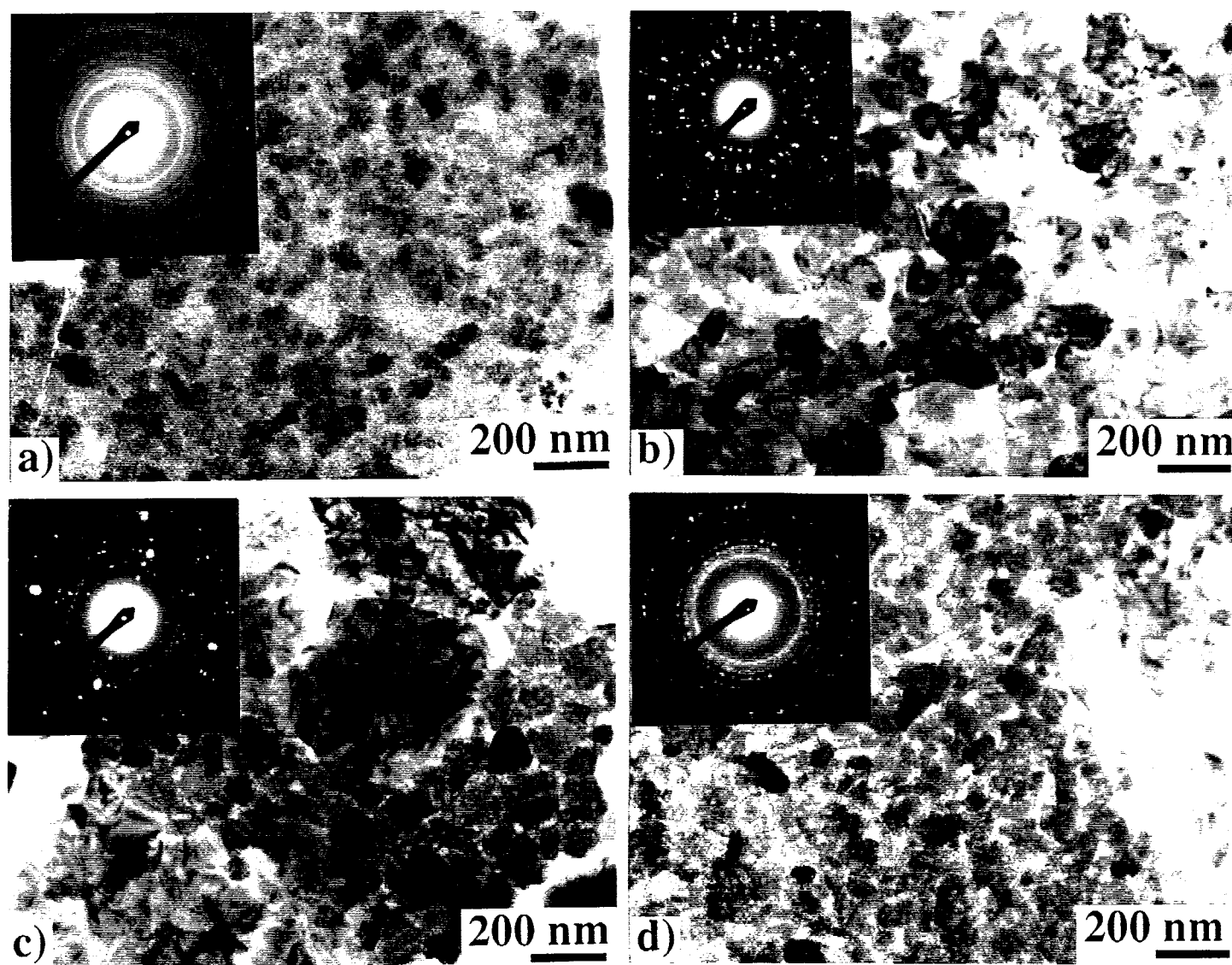


Figure 7. TEM micrographs of 40% Fe_2O_3 powders upquenched at (a) 800°C for 1 h and (b-d) 800°C for 24 h. Fine grain γ gives way to $\text{O}-(\text{Al,Fe})_2\text{O}_3$ and eventually to $\alpha_1 + \alpha_2$.

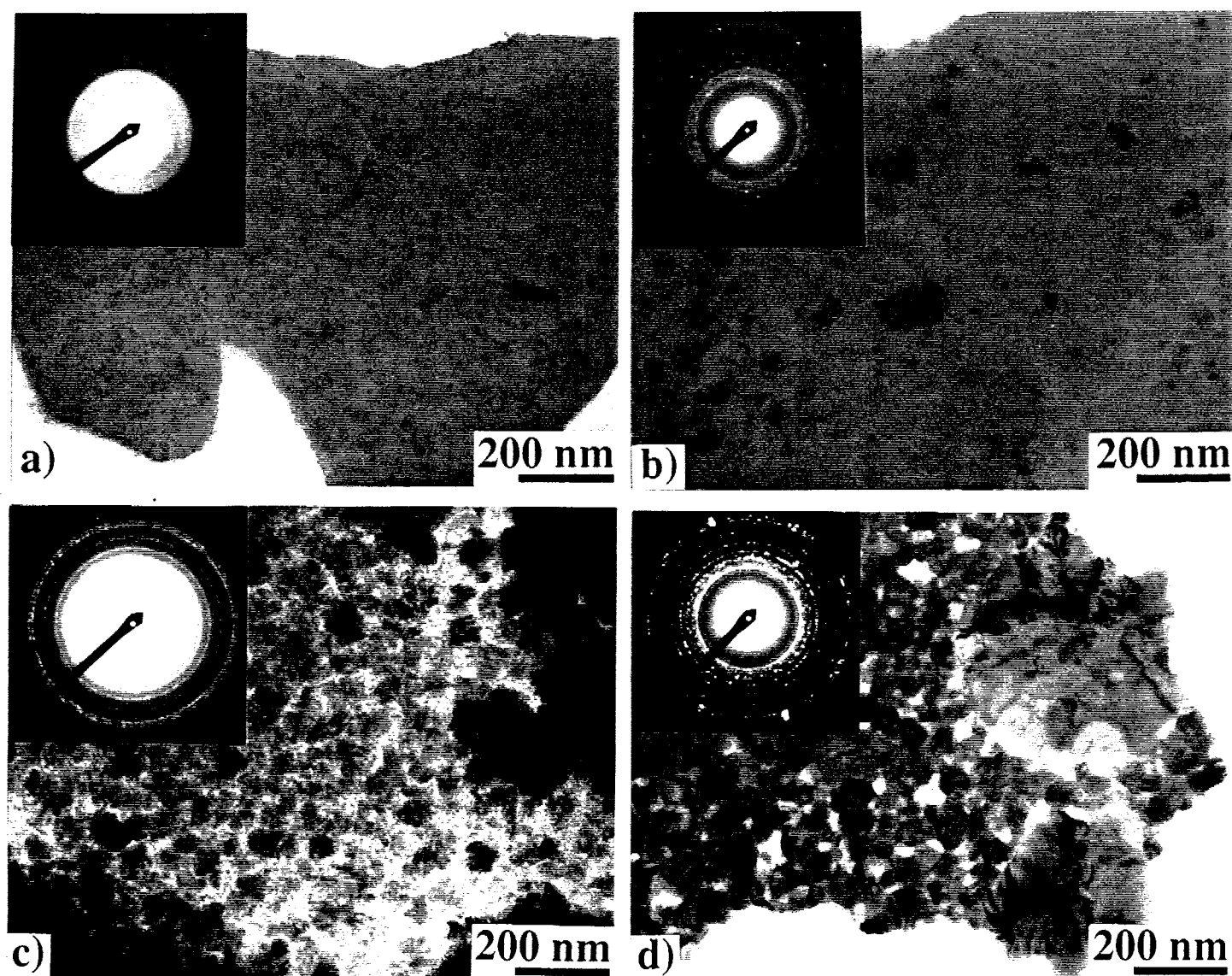


Figure 8. TEM micrographs of 50% Fe_2O_3 powder upquenched at (a) 700°C for 4 min., (b,c) 800°C for 20 min., and (d) 800°C for 24 h. $\alpha_1 + \alpha_2$ evolve from $\text{O-(Al,Fe)}_2\text{O}_3$ only for the longest treatment.

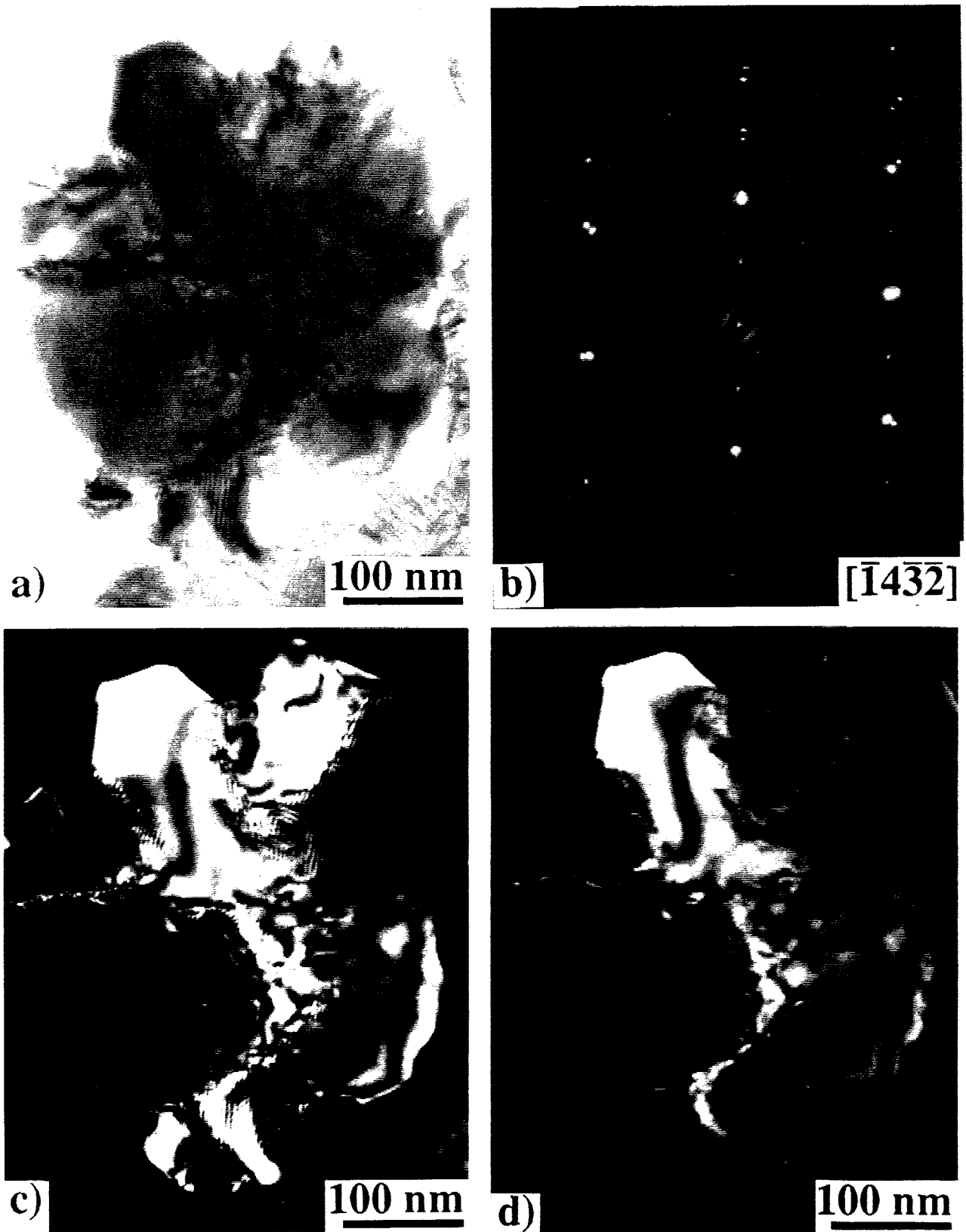


Figure 9. Dark field (DF) analysis of an α colony within the 50% Fe_2O_3 material. Micrographs show (a) a bright field image of an α colony, (b) the $[1\bar{4}32]$ zone axis diffraction pattern from the colony, (c) DF image using both spots indicated by arrow in (b), and (d) DF image from the spot closest to the central beam.

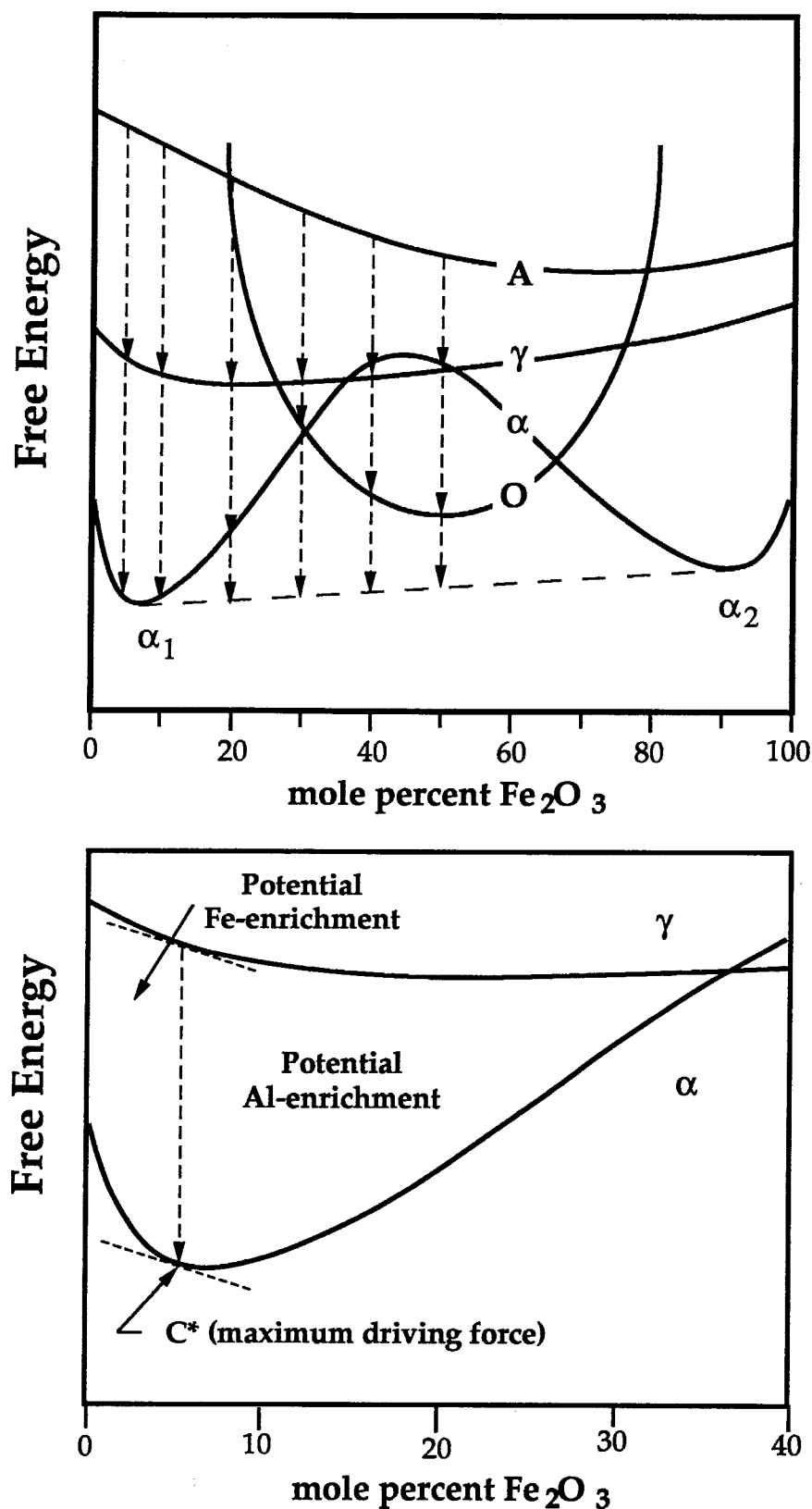


Figure 10. Schematic free energy diagram for the $\text{Al}_2\text{O}_3\text{-Fe}_2\text{O}_3$ system in the temperature range investigated. Arrows in (a) represent free energy changes corresponding to the observed transformation sequences. (b) depicts the composition ranges in which Fe or Al enrichment are favored during nucleation when limited diffusion is allowed.